ACS APPLIED MATERIALS & INTERFACES

www.acsami.org

Research Article

Asymmetric Superhydrophobic Textiles for Electromagnetic Interference Shielding, Photothermal Conversion, and Solar Water Evaporation

En Li,[§] Yamin Pan,[§] Chunfeng Wang, Chuntai Liu, Changyu Shen, Caofeng Pan, and Xianhu Liu*

Cite This: *ACS Appl. Mater. Interfaces* 2021, 13, 28996−29007

Read Online

ACCESS | Metrics & More | Article Recommendations | Supporting Information

ABSTRACT: Flexible and multifunctional textiles have potential applications in self-cleaning and portable electronic product applications, but the current problem that needs to be solved is to maintain their inherent breathability and flexibility while expanding other functional applications. Herein, we adopt the layer-by-layer assembly method to develop a multifunctional textile with superior asymmetric superhydrophobicity, excellent electromagnetic interference (EMI) shielding, outstanding photothermal conversion, and solar water evaporation. The synergistic effect of SiO_2 nanoparticles/poly(dimethylsiloxane) (PDMS) and 1*H*,1*H*,2*H*,2*H*-perfluorooctyltriethoxysilane (PFOTES) endows the textile with a water contact angle of 160°. MXene provides high conductivity (1200 S/m) and EMI shielding effects (36 dB) for multifunctional textiles. In addition, the multifunctional textile exhibits excellent photothermal conversion, and satisfactory solar water evaporation efficiency (80%) and rate (1.22 kg/(m^2 h)) under 1 sun. Therefore, the prepared multifunctional textile has great potential in multiscene applications.

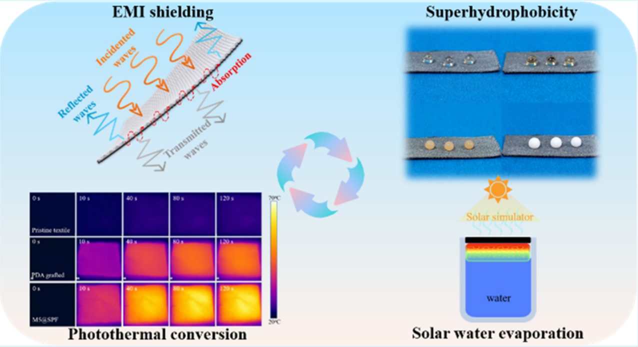

KEYWORDS: *electromagnetic interference shielding, photothermal conversion, textiles, superhydrophobicity, solar water evaporation*

1. INTRODUCTION

The vigorous development of the 5G era and the multifunctionality of miniaturized equipment have brought many benefits to humans. Meanwhile, the electromagnetic radiation generated by these devices brings in severe problems, causing serious interference and damage to electronic products and human health.[1−5] Due to the low cost, lightweight, and simple preparation, flexible and conductive textiles are widely used in energy storage,[6,7] electromagnetic interference (EMI) shielding,[8−10] sensors,[11−13] thermal management,[14−16] water evaporation, etc. There are many ways to prepare flexible textiles, such as dipping,[17] spraying,[18] stencil printing,[19] vapor spraying,[20] vacuum filtration,[21] and in situ growth.[22] However, the primary challenge now is to combine the inherent comfort, permeability, and porosity of textile substrates to develop new functionalities. Therefore, developing a multipurpose textile that can be applied to different environments is of great significance for broadening the application range of textiles.

Polymer textiles are widely used in our daily life and have the advantages of lightweight, flexibility, comfort, and permeability. They are considered to be ideal candidate substrates for the development of flexible, breathable, and multifunctional textiles.[23,24] Moreover, most of the polymer textiles are insensitive to electronic insulation and phonons, which allows them to be combined with conductive and photoresponsive materials for EMI shielding or photothermal heaters. To make up for the functional defects of polymer textiles, some materials such as metal nanoparticles,[25,26] carbon-based materials (graphene and carbon nanotubes),[27−32] and plasma nanoparticles or nanowires (Ag and AgNWs),[33,34] can be modified onto polymer textiles by spraying, vacuum filtration, dip-coating, electroless plating, in situ growth, and other strategies.

MXene is a unique two-dimensional (2D) transition metal carbide and/or nitride group $M_{n+1}X_nT_x$, where M is the early transition metal, X is carbon and/or nitrogen, and T_x is the end of the functional surface (such as −O, −F, and −OH).[35,36] The etching and delamination process introduces abundant surface terminal groups on the surface of the conductive MXene sheets, which makes it different from the inert surface of conductive graphene.[37−39] Thereby, MXene has excellent dispersibility in water and is more suitable for decorative

Received: April 29, 2021
Accepted: May 27, 2021
Published: June 8, 2021

https://doi.org/10.1021/acsami.1c07976

Scheme 1. Schematic Illustration of the Fabrication of Conductive and Superhydrophobic PET Textiles

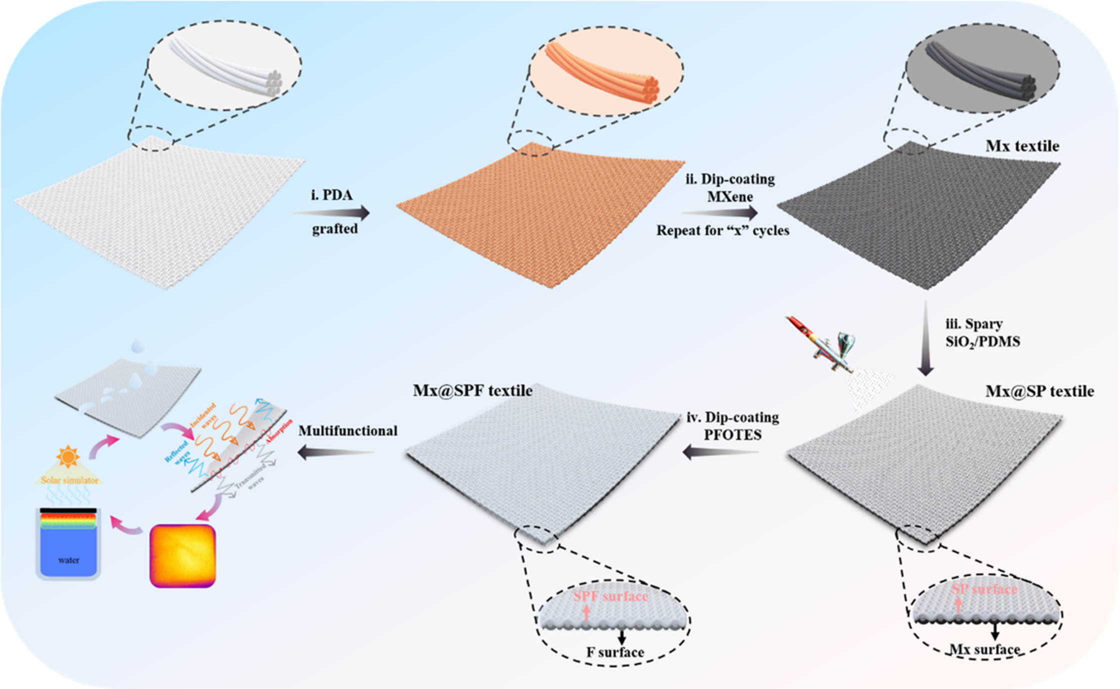

textiles.[40] Zhang et al. prepared a conductive and superhydrophobic silk textile for EMI shielding and humidity monitoring applications by a vacuum-assisted layered assembly method. The flexible multifunctional silk textile has a very low sheet resistance ($0.8\ \Omega\cdot sq^{-1}$) and an EMI shielding value of 54 dB, which is very sensitive to changes in humidity and maintains good air permeability and hydrophobicity.[33] Gao et al. fabricated a superhydrophobic, breathable, and elastic smart textile device with a multicore shell structure, which bonds MXene to the elastic textile through polydopamine (PDA) and was coated with poly(dimethylsiloxane) (PDMS). The designed smart textile electronics with superhydrophobicity ($CA \approx 151°$) and satisfactory air permeability have superior photothermal and electrothermal effects and can be used to detect human behavior due to its superior strain sensing performance.[41] However, MXene currently has the disadvantage of being easily oxidized when exposed to high humidity or even in air, which affects the stability of various properties. In addition, the functional expansion of MXene is also a relevant research direction, such as in the application of solar water evaporation.

Herein, we demonstrate a layer-by-layer assembly approach for fabricating superior conductive and asymmetric superhydrophobic polymer textiles with outstanding EMI shielding effectiveness (SE), photothermal conversion, and solar water evaporation performances. We utilized the adhesion of polydopamine (PDA) to decorate MXene on PET textile fibers. The mixed coating of hydrophobic fumed silica (Hf-SiO_2) and poly(dimethylsiloxane) (PDMS) endows superhydrophobic property to the textile and protects MXene from oxidation. To improve the robustness of Hf-SiO_2 nanoparticles, the outermost transparent coating 1*H*,1*H*,2*H*,2*H*-perfluorooctyltriethoxysilane (PFOTES) plays a great role. Thus, the two surfaces of the conductive PET textile have superhydrophobic properties with different adhesion properties and have potential applications in microdroplet transport. The PET textiles decorated with MXene are well investigated in terms of superhydrophobicity, EMI shielding, photothermal conversion, and solar water evaporation.

2. RESULTS AND DISCUSSION

2.1. Fabrication of Conductive and Superhydrophobic Multifunctional PET Textiles.

Scheme 1 shows a layer-by-layer assembly method for manufacturing multifunctional polymer textiles with outstanding electrical conductivity and superhydrophobicity. First, the PET textile matrix was treated with NaOH solution (10 wt %) to break the ester group on the macromolecular chain and introduced enough oxygen-containing groups to promote the subsequent loading of PDA. Then, the pristine textile was modified with PDA as an adhesive so that MXene was coated on the PET textile. Since PDA has a variety of functional groups, such as hydroxyl, amino, and catechol, the chemical activity of the inert textile can be achieved by modifying a layer of PDA on the surfaces of the polymer fibers.[42] After that, the modified PET textiles were immersed in the MXene solution under vacuum assistance to construct a conductive fiber network. The obtained textile is designated as M*x* textile, where *x* is the number of repetitions and M represents MXene. Finally, the SiO_2/PDMS suspension was evenly sprayed on one surface of the obtained conductive textile to make it superhydrophobic. The resulting textile is designated as M*x*@SP textile, where S and P represent SiO_2 and PDMS. Alternatively, to improve the robustness of SiO_2 nanoparticles and form a superhydrophobic surface with different properties on the back of the textile, we dipped the M*x*@SP textile into the PFOTES hydrolysate to form an M*x*@SPF textile with different superhydrophobic properties on both sides, where F represents the PFOTES.

As reported,[40] the $Ti_3C_2T_x$ MXene was synthesized following the layer delamination method by etching the Al layer of Ti_3AlC_2 with LiF/HCl solution. From Figure S1, it can be observed that the MXene aqueous solution has a typical

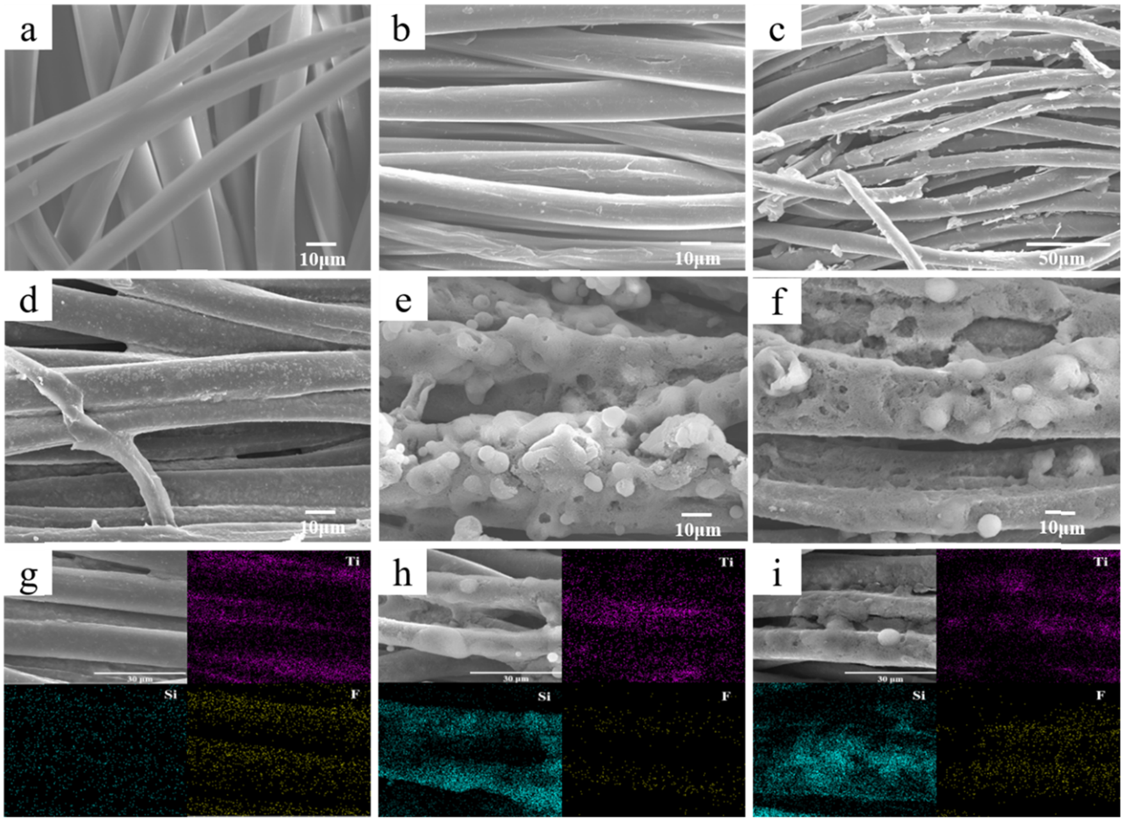

Figure 1. Scanning electron microscopy (SEM) images of (a) pristine textile, (b) PDA-grafted textile, (c) M5, (d) M5@F, (e) M5@SP, and (f) M5@SPF textile. (g−i) EDS elemental mapping images corresponding to d, e, and f, respectively.

Tyndall effect. The surface of MXene is rich in hydroxides and fluorine groups, which make it evenly disperse in water. As shown in the Fourier transform infrared (FTIR) spectra (Figure S2), after PDA was grafted onto PET fibers, the disappearance of the corresponding $-CH_3$, $-CH_2$, and $-N-H$ groups at 2922, 2851, and 1594 cm^{-1} proved the successful grafting of PDA. After coating with MXene, the peaks at 1715, 1505, 1237/1092, and 1016 cm^{-1} corresponding to the carbonyl group, benzene ring skeleton, ester group, and alcohol group were weakened. It is different from the M5 textile in that the peak of $-C-H$ out-of-plane bending vibration corresponding to 770 cm^{-1} reappears due to PDMS or PFOTES. From the FTIR results, the successful preparation of superhydrophobic and multifunctional PET textiles was proved.

Compared with the smooth pristine PET textile (Figure 1a), obvious roughness was observed for the PDA-grafted PET fibers (Figure 1b). We can clearly observe the uniform distribution of C, N, and O elements on the surface of the fibers from the energy-dispersive spectrometry (EDS) elemental mapping images (Figure S4). As shown in Figure 1c, MXene nanosheets are densely dispersed and wrapped on the surface of the fibers. Obviously, as the number of dip-coating increases, the MXene content increases correspondingly between the fiber surface and the fiber gap (Figure S3). Irregular micro−nano particles appeared on the surface of MXene-wrapped fibers after dipping in PFOTES hydrolysate (Figure 1d). The presence of these particles formed micro−nano structures, which is also the source of the superhydrophobic ability of M5@F textiles. After spraying the SiO_2/PDMS suspension, the surface roughness of the fibers increased sharply, and large agglomerated spheres of nano SiO_2 particles appeared under the condition that PDMS tightly wrapped the fibers (Figures 1e and S5). From the EDS elemental mapping images of M5@F, M5@SP, and M5@SPF fibers, all three highlight the distribution of Ti elements and prove the uniform distribution of MXene nanosheets (Figure 1g−i). The distribution of F elements on the surface of M5@F and M5@SPF fibers confirms the presence of the PFOTES coating. A large amount of Si elements on the surface of M5@SP and M5@SPF fibers are due to SiO_2/PDMS.

2.2. Superhydrophobicity Behavior of Multifunctional PET Textiles.

To prevent the oxidation of MXene and ensure its long-term stability and durability, surface modification of multifunctional textiles is a common method. As shown in Figure 2a, the pristine textile, PDA-grafted textile, and coated with MXene (M*x* textile) are all completely superhydrophilic. Water can be absorbed quickly after contact due to the fact that PDA and MXene contain a large number of hydrophilic groups. After PFOTES coating, the hydrophilic surface is converted to a hydrophobic surface with a water contact angle (WCA) of up to 149°. It is noted that PFOTES has almost no effect on the surface morphology and color of the textiles (Figure 1d). In contrast, the WCA of the surface of the M5@SP textile is larger than 150°. This is because the micro−nano structure is formed on the surface of the fibers, according to the Cassie model.[43,44] The WCA of the multifunctional textile was significantly increased with the synergy of SiO_2/PDMS and PFOTES, and the WCA was up to 160° for the SPF surface of M5@SPF textile. The improvement in the WCA may be attributed to the construction of a robust layered protrusion structure with an appropriate

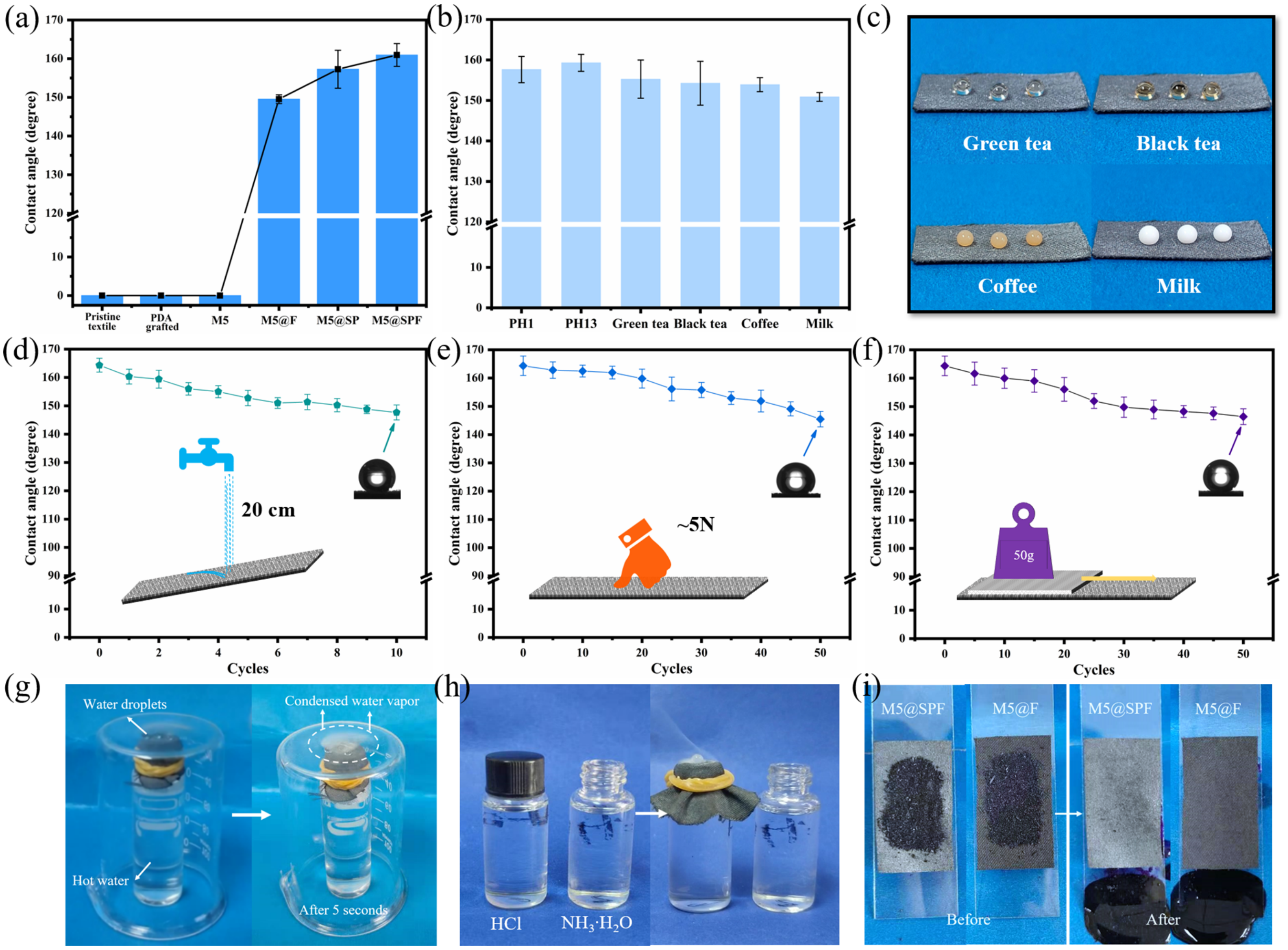

Figure 2. (a) WCAs of the PET textiles after different treatments. (b) WCA of the M5@SPF textile in different solutions and (c) the corresponding optical images. Variation of WCA for the M5@SPF textile under (d) water flow impact, (e) finger press, and (f) sandpaper abrasion. The inset shows the schematic illustration of the robustness test. Optical images showing (g) water vapor transmission performance and (h) HCl gas permeating from the glass bottle covered with the M5@SPF textile. (i) Self-cleaning performance of the surface of M5@F and M5@SPF textiles.

combination of particles of different sizes on the surface of the textile.[45] Interestingly, after spraying SiO_2/PDMS and dip-coating PFOTES on the Mx textile, the WCA was not significantly affected by the dip-coating times of MXene (Figure S6). The superhydrophobicity of the multifunctional textiles remains almost unchanged when facing corrosive media (PH1, PH13). However, WCA decreased slightly when the textiles were exposed to common solutions used in our daily life, but their WCA values were all larger than 150° (Figure 2b). As shown in Figure 2c, water droplets of different solutions adhere to the surface of the multifunctional textiles and maintain a completely spherical shape. In practical applications, the superhydrophobic surface of multifunctional textiles may be affected by the harsh environment and lose its superhydrophobic properties.[46] Therefore, a series of tests were carried out to measure the mechanical robustness of superhydrophobic textiles, such as water flow impact, finger press, sandpaper abrasion, etc. After 5 cycles of water flow impact (each cycle = 1 min), the superhydrophobic surface of the textile still maintains superhydrophobicity with a WCA of 154°. After 10 cycles, the WCA of the textile was reduced to 148° but still has satisfactory water repellency (Figure 2d and Movie S1). The WCA change records of the superhydrophobic surface of the M5@SPF textile in different finger pressure cycles are shown in Figure 2e. The results showed that WCA decreased slowly with the increase of the number of cycles, and remained at 145° after 50 cycles of finger press, indicating that the superhydrophobic textile can maintain hydrophobicity after skin contact. After 20 cycles of more destructive sandpaper abrasion (the movement of 2 cm with a weight of 50 g is defined as a cycle), the surface of the superhydrophobic textile with WCA of 155° still maintained excellent superhydrophobicity (Figure 2f). Then, it decreased significantly until the WCA was 146° after 50 cycles. It is worth noting that the water droplets still exhibit a nearly spherical shape and are not absorbed by the textile after the superhydrophobic layer was severely damaged.

From the SEM images, we can note that the MXene nanosheets and SiO_2/PDMS are mostly adsorbed on the surface of the fibers instead of the large gaps between the fibers to obtain superhydrophobicity while maintaining air permeability. As shown in Figure 2g and Movie S2, the superhydrophobic textile was tied to the opening of the glass bottle in a beaker by a rubber band. Obviously, the water vapor can escape from the glass bottle containing hot water and pass through the asymmetric superhydrophobic textile from the F

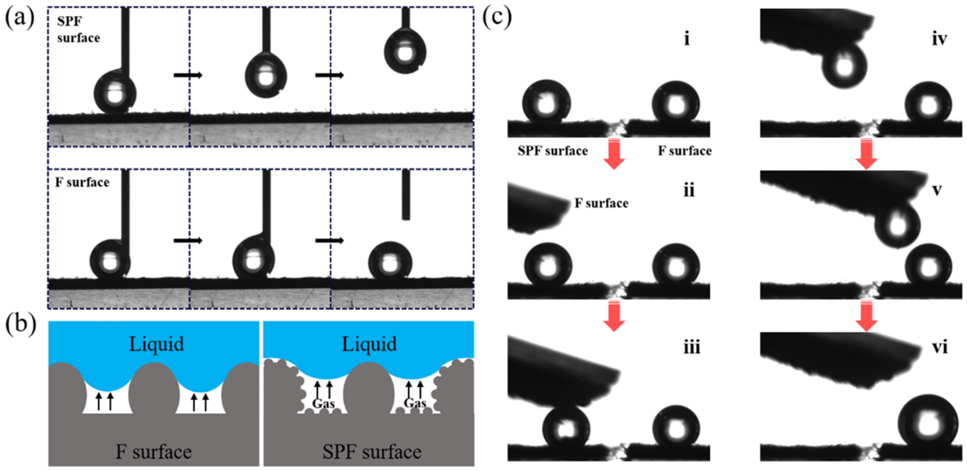

Figure 3. (a) Optical images of dynamic measurements of water adhesion on the SPF and F surfaces. (b) Schematic representation of the structure of F and SPF surfaces. (c) The almost nondestructive transfer process of the microdroplet. Water droplets are placed on two surfaces of the M5@SPF textile. The water drop on the left is captured by the F surface and it is transferred and mixed with the water drop on the right.

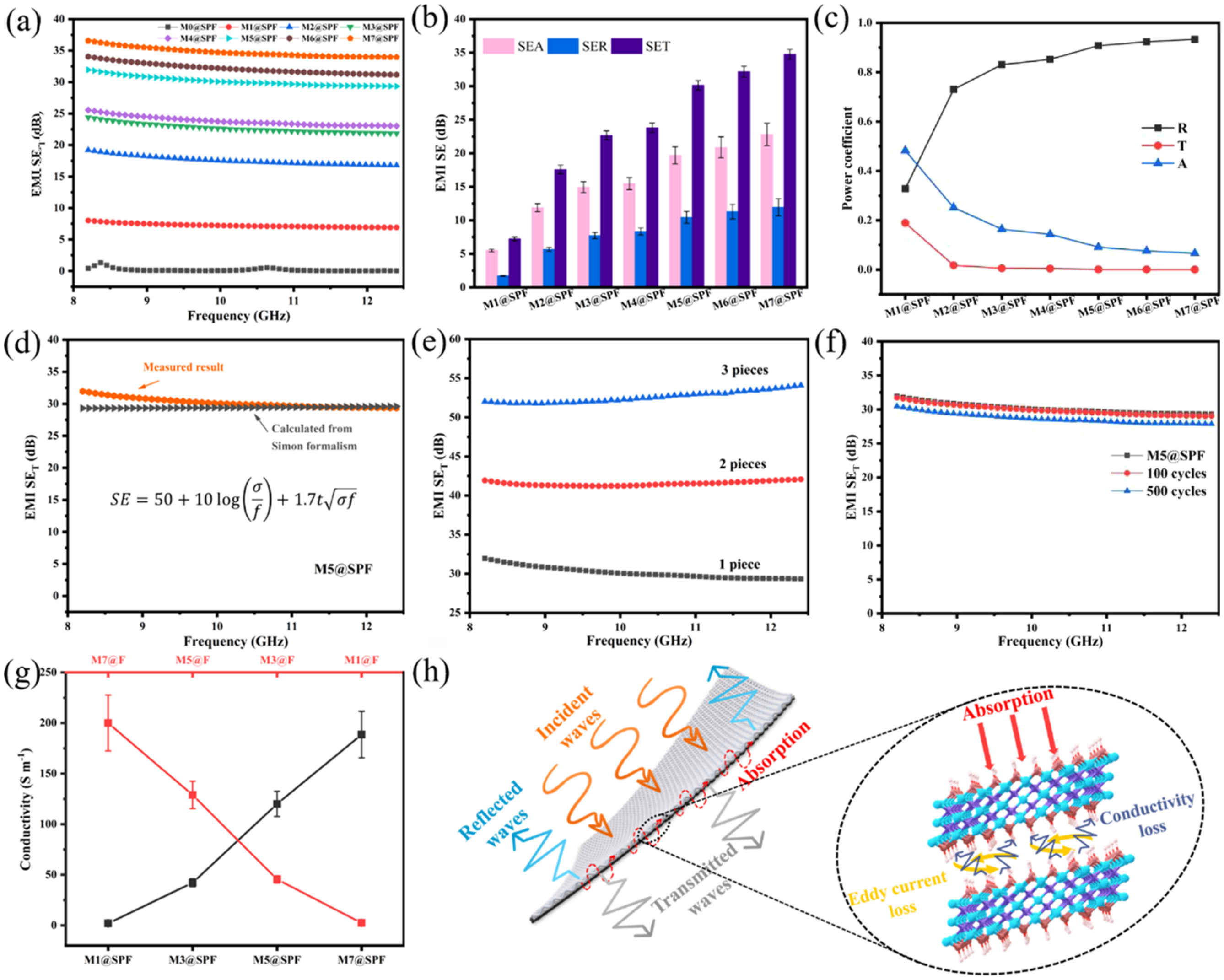

Figure 4. (a) EMI SE$_T$ versus frequency and (b) average SE$_T$, SE$_A$, and SE$_R$ values of the M*x*@SPF textile in the X band. (c) The power coefficients of reflectivity (*R*), absorptivity (*A*), and transmissivity (*T*) values of the M*x*@SPF textile. (d) The theoretical EMI SE$_T$ value of conductive textile (200 μm thick) calculated by Simon's formula is closely related to the experimental results. (e) The EMI SE of different pieces of the M5@SPF textile. (f) The stability of the EMI SE$_T$ value of the M5@SPF textile after a large number of bending times. (g) Electrical conductivity of M*x*@F and M*x*@SPF textiles. (h) Schematic illustration of the EMI shielding mechanism of the M*x*@SPF textile.

side to the SPF side after 5 s, and finally, condense to water in the beaker. Similarly, hydrochloric acid gas can also pass through the asymmetric superhydrophobic textile and generate white smoke above it (Figure 2h and Movie S3) (hydrochloric acid is released from the glass bottle and reacts with ammonia to produce ammonium chloride). All of the above proves that the superhydrophobic textile has excellent water vapor permeability. In addition, self-cleaning performance is also observed in asymmetric superhydrophobic textiles (Figure 2i and Movie S4). The two surfaces of M5@SPF (SPF and F sides) were contaminated by potassium permanganate powder and then attached to the glass slide inclined at the same slope. Obviously, due to the presence of water droplets, the potassium permanganate powder on the SPF surface has been completely removed, leaving the textile surface in its pristine state. However, there were traces of droplets doped with potassium permanganate on the F surface. The results show that the adhesion of water droplets on the SPF surface is much lower than that on the F surface. Corresponding to the results shown in Figure 3a, the syringe can easily carry water droplets away from the SPF surface during the ascent. In contrast, the same volume of water droplet leaves the syringe and stays on the F surface. The surface of superhydrophobic materials with different wettabilities has a wide range of potential applications in droplet manipulation.[47] The schematic representation of the surface structure is shown in Figure 3b. Due to the presence of larger micron particles on the F surface, the F surface has a larger contact area with the droplets, resulting in strong adhesion to the droplets. However, the micro−nano structure formed by the SiO_2 nanoparticles and PFOTES microparticles leads to a reduction in the contact area between the SPF surface and the droplets, causing the SPF surface to have a weaker adhesion to the droplet.[48] Figure 3c shows the almost lossless transfer and mixing of microdroplets using the SPF surface and the F surface. The F surface has high adhesion and could be used as a microdroplet catcher to capture the microdroplet on the left SPF surface. Subsequently, the microdroplet comes into contact with another microdroplet on the right F surface. Under the action of the volume and gravity of the microdroplet, the newly generated microdroplet leaves the capture and mixes with the microdroplet on the right F surface. The coated SiO_2/PDMS on the surface of the textiles endows them with superhydrophobic properties with low adhesion. However, the presence of PFOTES increased the robustness of SiO_2 nanoparticles and also provided a hydrophobic surface with high adhesion.

2.3. Electrical and EMI Shielding Performances of Multifunctional PET Textiles. The content of MXene can be controlled by adjusting the number of dip-coatings of the textile in the MXene solution (8 mg/mL). Generally, as the content of MXene and the number of dip-coatings increase, the conductivity and EMI shielding performance of the textile increase accordingly (Figure 4a,g). As the number of dip-coatings increased from 1 to 7 cycles, the EMI SE of the Mx@SPF textile increased from 8 to 36 dB. As shown in Figure 4b, the increase in conductivity leads to an enhancement in absorption (SE_A) and reflection (SE_R). According to the Fresnel equation, SE_A and SE_R are directly proportional to conductivity.[49,50] Interestingly, the increase of SE_A is greater than the increase of SE_R, and SE_R is saturated in the range of 10−15 dB, while SE_A is still increasing. This corresponds to a different mathematical relationship between SE_A/SE_R and conductivity: SE_R is proportional to the logarithm of conductivity (σ), and so, the change in $SE_R$with σ is small. However, SE_A is proportional to the square root of σ, and so, a small increase in σ will cause a large change in SE_A, which is the main reason for the exponential attenuation of incident electromagnetic waves (EMWs) due to current loss and eddy current loss.[51] To analyze the shielding mechanism of the Mx@SPF textile, the absorption coefficient (A) and reflection coefficient (R) were calculated from the scattering parameter S (Figure 4c). For all Mx@SPF textiles, the R-value is much higher than the A-value, except for M1@SPF textile (Figure 4c), indicating that due to impedance mismatch, all Mx@SPF textiles are highly reflective materials, which means that high conductivity Mx@SPF textiles can reflect most of the incident EMWs and only a small amount of EMWs can penetrate the material. From the above results, it can be noted that most of the incident EMWs are reflected first before being absorbed. The incident EMWs penetrating into the Mx@SPF textile are efficiently attenuated by the internal conductance loss and internal reflection, which means that the contribution of SE_A to the total EMI SE is dominant. The Simon formalism ($\mathrm{SE} = 50 + 10\log\left(\frac{\sigma}{f}\right) + 1.7t\sqrt{\sigma f}$, where σ (S/cm), t (cm), and f (MHz) are the electrical conductivity, sample thickness, and frequency, respectively.) is usually used to predict the EMI SE value of thin-film materials in the X band.[52,53] As shown in Figures 4d and S7, the theoretical EMI SE value obtained by the Simon formalism is the approach to measure the EMI SE value of the Mx@SPF textile with a thickness of 200 μm in the X-band.

The thickness also acts as a barrier to the process of EMWs entering the material, and textiles are generally used in multiple layers. The EMI SE is increased to 42 and 53 dB by stacking two and three pieces of the M5@SPF textile (Figure 4e). The bending of textiles is inevitable. After 100 and 500 cycles of bending, the EMI SE decreases by about 0.5 and 2 dB, which shows the integrity of the conductive network of the M5@SPF textile and the stability of the EMI shielding performance. The high EMI SE is mainly due to the high conductivity of the MXene nanosheets wrapped in the fiber network.[54] Figure S8, respectively, shows the relationship between conductivity and content with the dip-coating cycle of MXene coated on PET textiles. As the textile has a strong wicking effect, both of them increase rapidly with the increase in the number of dip-coating cycles. However, the electrical conductivity of the textiles decreased significantly after the hydrophobic treatment. Figure 4g shows the changes in conductivity with the number of dip-coating cycles after treatment with two different superhydrophobic properties. Obviously, the presence of SiO_2/PDMS decreases the conductivity slightly than the single PFOTES coated textile. Nevertheless, the EMI SE and conductivity values obtained are relatively outstanding in performance compared to most reported EMI shielding textiles (Table S1). The schematic illustration of the EMI shielding mechanism of Mx@SPF textiles is shown in Figure 4h.

2.4. Photothermal Conversion Property of Multifunctional PET Textiles. Wearable multifunctional textiles have an outstanding photothermal conversion property under the synergistic effect of MXene and have potential applications in personal thermal management.[55] Therefore, we conducted a detailed study of Mx@SPF textiles on the photothermal conversion characteristics. The tested sample (5 cm × 5 cm) is placed on the white platform under the solar simulator, and the power density is determined in advance by the power density

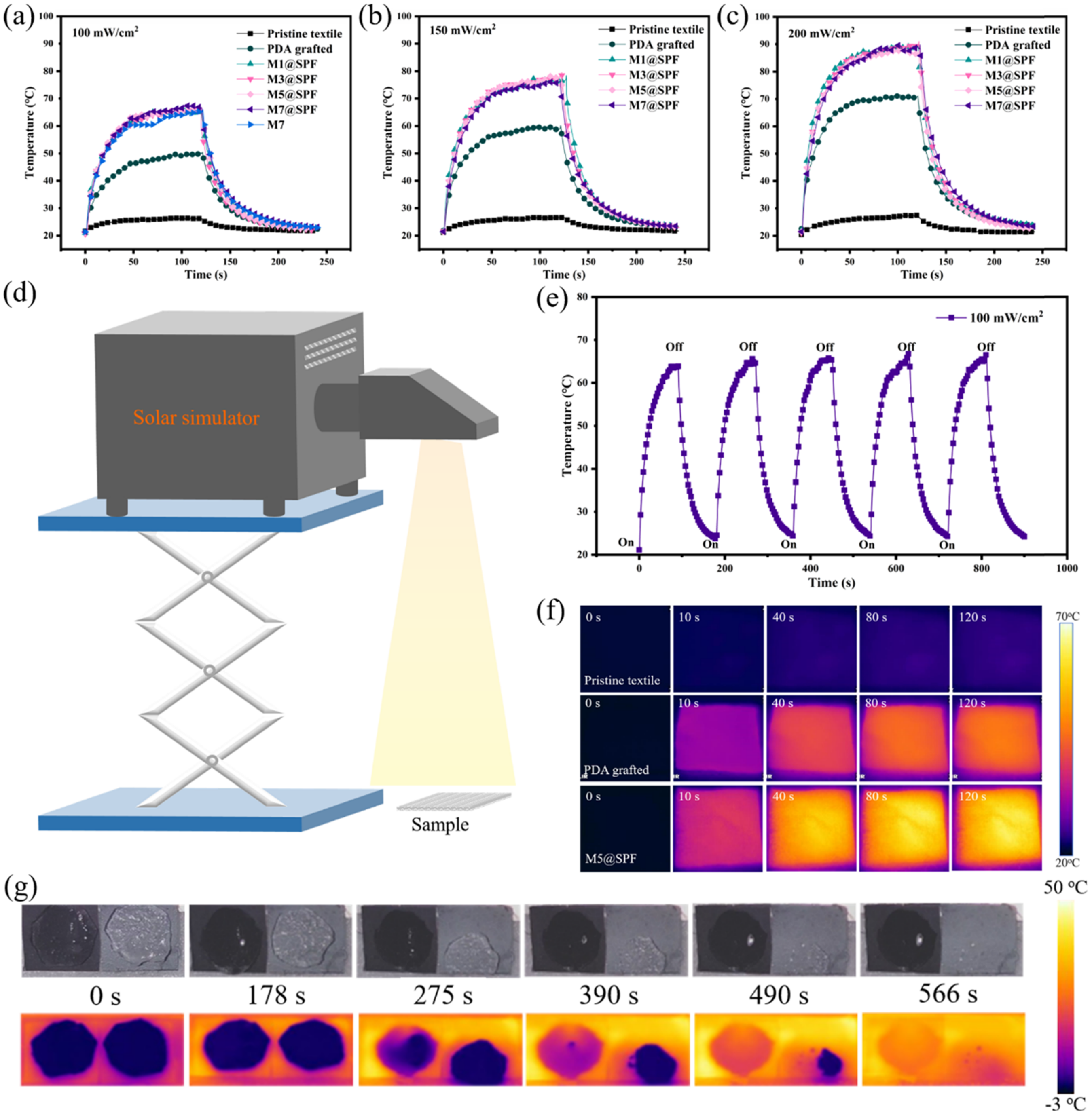

Figure 5. Surface temperature−time curve of PET textiles at power densities of (a) 100 mW/cm^2, (b) 150 mW/cm^2, and (c) 200 mW/cm^2. (d) Schematic illustration of the photothermal conversion of M*x*@SPF textiles under the solar simulator. (e) Surface temperature−time curve of M5@SPF textiles under repeated heating/cooling cycles. (f) IR images corresponding to the surface temperature−time of the pristine textile, PDA-grafted textile, and M5@SPF textile at a power density of 100 mW/cm^2. (g) IR and optical images of the F and SPF surfaces of M5@SPF textiles during the deicing process at a power density of 100 mW/cm^2.

meter (Figure 5d). Figure 5a−c shows the temperature−time curve of M*x*@SPF textiles under different power densities, respectively. The results show that the surface temperature of all textile samples can increase quickly and reach an equilibrium value, and rapidly decrease to the ambient temperature after removing the light source. Interestingly, the equilibrium temperature of M*x*@SPF textiles did not improve with the increase in the dip-coating times of MXene but was significantly higher than that of pristine textile and PDA-grafted textile with the same power density. This could be due to the fact that the “blackness” of the textile had reached saturation after MXene coating. Moreover, the absorption of M*x*@SPF textiles was not significantly affected by the dip-coating times of MXene under the standard solar spectrum of air mass 1.5 global (Figure S9). Figure 5e shows the repeated photothermal heating and cooling curve of Mthe5@SPF textile with a power density of 100 mW/cm^2, which highlights its stability and rapid response in reusable and long-term operation. The pictures and infrared (IR) images of the textiles in Figure 5f show the temperature distribution of

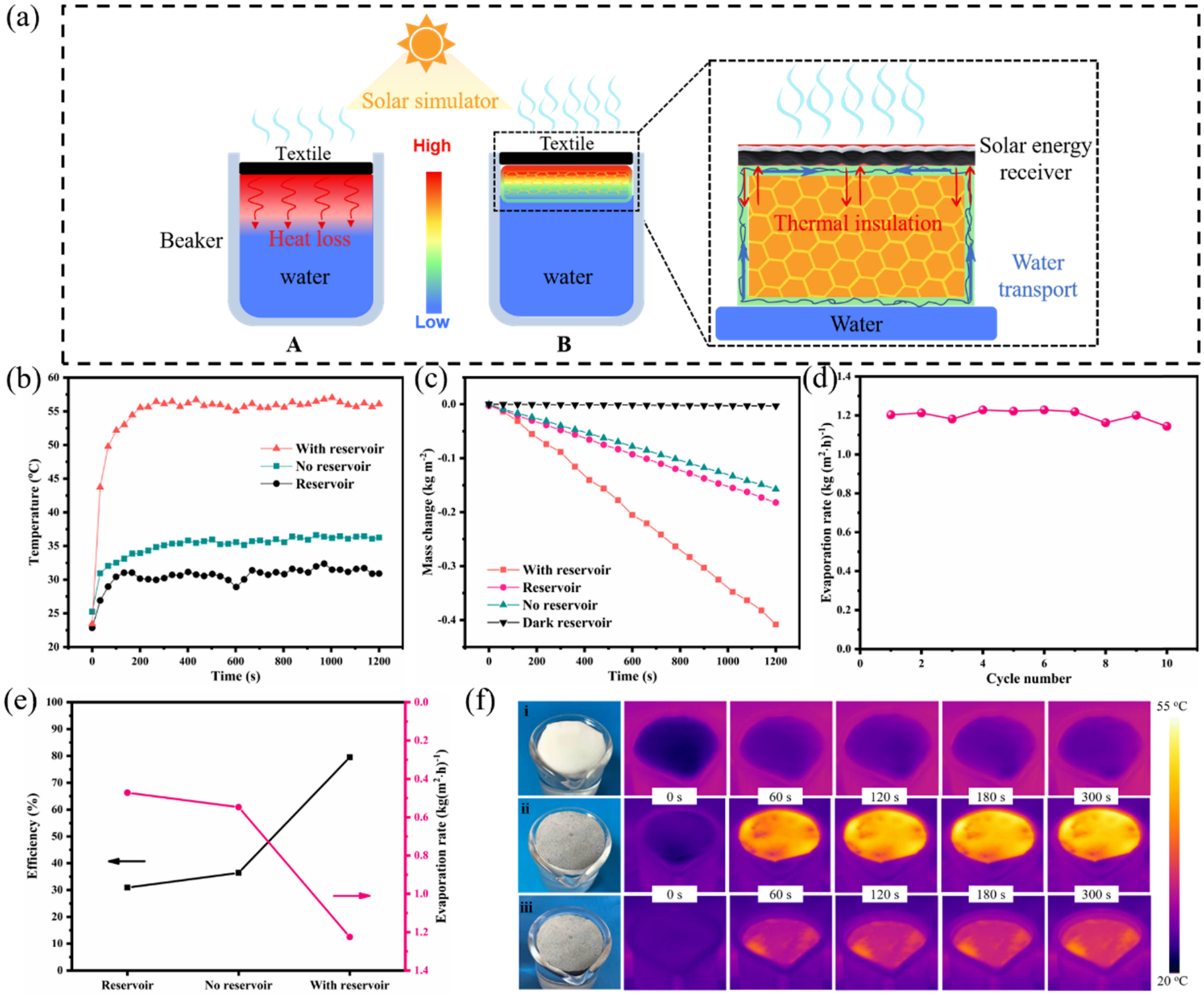

Figure 6. (a) Schematic illustration of solar water evaporation (A) device in direct contact with bulk water, and (B) with thermal insulation and rapid water transporting ability. (b) The surface temperature and (c) mass change of water over time for the separate reservoir, and the M3@SPF textile with reservoir and no reservoir. (d) Evaporation cycle performance of solar water evaporation devices over 10 cycles. (e) Solar vapor conversion efficiencies and the evaporation rates of the solar vapor generation devices based on the M3@SPF textile. (f) Time-dependent IR images of the separate reservoir (i), and M3@SPF textile with reservoir (ii) and no reservoir (iii). The power density is 100 mW/cm^2.

the textile with different treatments. According to a previous report, the ice detention effect was found on the superhydrophobic coating, which is due to the air cushion (Cassie model) between the water droplet and the superhydrophobic surface reducing the heat transfer between the water and the coating.[56] Hence, we designed a deicing simulation experiment to remove ice cubes (1 cm^2 × 2 mm) on the two surfaces of M5@SPF (F and SPF surfaces), and then put them on a solar simulator with a power density of 100 mW/cm^2 at the same time (Figure 5g). Obviously, the ice on the F surface completely melted within 490 s, while the SPF surface still had unmelted ice. However, the difference is that the ice cube on the SPF surface slipped slowly during the melting process, and finally, melted completely at 566 s but the F surface had the smooth water droplets intact.

2.5. Solar Water Evaporation Performance of Multifunctional PET Textiles.

Broadband and efficient solar energy absorption to effectively generate vapor while minimizing parasitic heat loss are the main two factors for achieving efficient solar steam generation. As shown in Figure 6a-A, to ensure the received solar energy can be effectively transferred to the bulk water to produce vapor, the receiver is always in direct contact with the bulk water. However, a large part of the energy will be dissipated due to the thermal conductivity of water, and the energy cannot be concentrated to heat the local bulk water. Here, we demonstrate a water vapor generating device that integrates the M*x*@SPF textile with a support structure (reservoir) with water transport, which can suppress heat loss (Figure 6a-B). The support structure is a cylinder composed of thin cotton wrapped around the polystyrene foam. The support structure was covered with cotton floats on the surface of the reservoir, and the bottom was in direct contact with bulk water. The capillary force of cotton was used to transport the water in the reservoir from the bottom to the top. In addition, the water in the reservoir was transported to the top in one direction, and the water heated by solar energy cannot be returned to the reservoir. The SPF surface of the M3@SPF textile was at the top and the F surface was at the bottom.

Figure 6b shows the surface temperature−time curve of the separate reservoir and M3@SPF textile with and no reservoir under 1 sun (100 mW/cm^2). For the M3@SPF textile, the surface temperature increases from room temperature to the plateau temperature (55 °C) within 200 s and reaches the plateau temperature (35 °C) within 300 s with no reservoir. For the separate reservoir, the surface temperature only reached 30 °C, and the temperature curve was unstable. The corresponding optical and IR images are shown in Figure 6f. As shown in Figure S10, the water mass changes of the M3@SPF textile are better than others. However, the water mass changes of the M7@SPF textile with the most MXene dip-coating times have the least changes. The results show that the M3@SPF textile could exert outstanding heat conduction and photothermal conversion effects while maintaining excellent air permeability. Figure 6c corresponds to the water mass change of Figure 6b and the spontaneous water evaporation mass change produced by the separate reservoir under dark conditions. To ensure that the water evaporation produced is only the result of solar exposure, we subtracted the evaporation rate of the separate reservoir at room temperature and darkness. Obviously, the M3@SPF textile with reservoir has the fastest water evaporation rate (1.22 kg/(m^2 h)) (Movie S5). Corresponding to the results in Figure 6c, the water evaporation rate of the M3@SPF textile in direct contact with bulk water (0.55 kg/(m^2 h)) is slightly higher than that of the separate reservoir (0.47 kg/(m^2 h)). Combining the water conduction and heat loss in the above two different situations, the slightly higher surface temperature of the M3@SPF textile with no reservoir occupied a leading position. As shown in Figure 6d, the M3@SPF textile with reservoir still has a stable water evaporation rate after 10 cycles. The solar water evaporation rate and efficiency of the separate reservoir, M3@SPF textile with and without reservoir, are shown in Figure 6e. The solar water evaporation efficiency (η) of the M3@SPF textile with reservoir was 80%, which was calculated by the following equation[57,58]

$$\eta = \frac{\dot{m}h_{\mathrm{LV}}}{C_{\mathrm{opt}}P} \times 100\%$$

where $\dot{m}$ is the solar water evaporation rate under the steady state (kg/(m^2 h)), h_{LV} is the sum of enthalpy for the liquid-vapor phase change, calculated from the surface temperature of the sample,[57] C_{opt} is the optical concentration, and P (= 100 mW/cm^2) is the solar power density. The M3@SPF textile with no reservoir device produced a solar water evaporation conversion efficiency of 36% (Figure 6e), which is significantly higher than that of a separate reservoir device (31%) due to the local heat generated by the M3@SPF textile converted from absorbed solar energy. In general, the above results demonstrated the importance of local heating and water delivery regulation in solar water evaporation systems.

3. CONCLUSIONS

We demonstrate a layer-by-layer assembly approach for the preparation of asymmetry superhydrophobic textiles with outstanding EMI SE, photothermal conversion property, and solar water evaporation performance. The 2D MXene nanosheets are assembled on PET textile fibers under the action of PDA to generate conductive textiles. After the asymmetric hydrophobic treatment, the textile has robust water repellency (WCA ≈ 160°), which can prevent the oxidation of MXene and does not affect the air permeability of the textile. Owing to the completely different adhesion between the SPF and F surfaces, the microdroplets can be transferred from the two surfaces almost without loss. The multifunctional textile not only exhibits excellent EMI SE (36 dB) but also presents outstanding photothermal conversion property, and hence, the textile has potential applications in the field of solar water evaporation. The multifunctional textile has a satisfactory solar water evaporation efficiency (80%) and rate (1.22 kg/(m^2 h)) under the action of local heating and reservoir. The designed multifunctional textile provides a path for the practical application of textiles in EMI shielding and advances a general guideline for the exploration of photothermal conversion and solar water evaporation.

4. EXPERIMENT SECTION

4.1. Materials. Ti_3AlC_2 MAX powders were provided by Jilin 11 Technology Co., Ltd. Lithium fluoride (LiF, 99%), 1*H*,1*H*,2*H*,2*H*-perfluorooctyltriethoxysilane (>97%; PFOTES), tris(hydroxymethyl)aminomethane (99.9%), and dopamine hydrochloride (98%) were provided by Shanghai Aladdin Biochemical Technology Co., Ltd. Hydrogen chloride (HCl) was obtained from Sinopharm Chemical Reagent Co., Ltd. Ethanol (C_2H_5OH) was obtained from Tianjin Damao Chemical Reagent Co., Ltd. Hf-SiO_2 (110 m^2/g specific surface area, 16 nm diameter, and 0.6−1.2 wt % carbon content) was purchased from Evonik Industries Co. Ltd., Germany. PDMS (Sylgard 184) and the curing agent were purchased from Dow Corning. PET textiles were bought from Jiangsu Qingxin Textile Factory.

4.2. Synthesis of $Ti_3C_2T_x$ MXene. The $Ti_3C_2T_x$ MXene sheet was synthesized by etching Ti_3AlC_2 powders by the method introduced in the previous report.[59] Briefly, 2 g of LiF was added to 40 mL of HCl (9 M) in a Teflon container and stirred for 30 min. Then, 2 g of Ti_3AlC_2 powders were then slowly added into the mixed solution. The mixture was stirred for 24 h (400 rpm) at 35 °C. The resultant MXene was washed with deionized (DI) water and centrifuged at 3500 rpm until the pH of the supernate was about 6. Then, the obtained MXene sediment was intercalated in ethanol accompanied by ultrasonic exfoliation for 1 h. The delaminated $Ti_3C_2T_x$ suspension was obtained by centrifuging at 3500 rpm for 3 min. The delaminated $Ti_3C_2T_x$ MXene sheets were obtained after 72 h of freeze-drying at −78 °C.

4.3. Synthesis of PET Textiles Coated with MXene. At first, the pristine PET textile was treated with NaOH solution (10 wt %) at 80 °C for 2 h to break ester groups and then washed with DI water several times. Then, the pristine PET textile was soaked in dopamine solution for 6 h at room temperature. The dopamine solution was obtained by dissolving 0.24 g of Tris powder and 0.4 g of dopamine hydrochloride in deionized water as reported.[41] After drying at 60 °C, the pristine PET textiles were dipped in MXene solution (8 mg/mL) for 10 min, followed by vacuum assistance, and then dried at 50 °C in a vacuum oven. The content of MXene in the textiles was adjusted by repeating the dip-coating. For convenience, the obtained PET textile coated with MXene was named Mx textile, where *x* (wt %) was the mass fraction of MXene solution.

4.4. Synthesis of MXene Textiles Decorated with Hf-SiO_2/PDMS/PFOTES. PDMS (1.5 g) was first dissolved in 15 mL of anhydrous ethanol. Then, 1 g of Hf-SiO_2 (16 nm, 110 m^2/g) was added, and the mixed solution was ultrasonicated at 120 W for 1 h. Subsequently, the curing agents of PDMS (0.15 g) were added to the solution. Afterward, the SiO_2/PDMS dispersion was continuously sprayed on one side of the PET textile at a speed of 0.5 cm/s using a commercial spray (Airbrush WeiYi HD180), followed by curing at 80 °C for 30 min. The obtained SiO_2/PDMS-decorated MXene textile was named Mx@SP textile with x representing the mass fraction of MXene. Furthermore, 1 mL of PFOTES was dissolved in 50 mL of anhydrous ethanol and left at room temperature for 1 h for the complete hydrolysis of PFOTES. Then, the Mx@SP textile was soaked in PFOTES solution for 1 h, followed by drying at 60 °C for 6 h. For convenience, the obtained superhydrophobic textile was named Mx@SPF textile.

4.5. Characterization. The surface structure and morphology of the multifunctional PET-based textiles were characterized by a field emission scanning electron microscope (FE-SEM, JSM-7001F). FTIR spectroscopy was performed in the range of 400−4000 cm^{-1} using a spectrometer (Thermo Fisher Nicolet 6700). The electrical conductivity of multifunctional PET-based textiles was measured using a Loresta-GP meter with a four-pin probe. The contact angle (CA) of textiles was measured with an SL200KS goniometer. The EMI SE was measured using a two-port vector network analyzer (Agilent N5244A) within 8.2−12.4 GHz. The reflection factor (R) and transmission factor (T) were calculated using $R = |S_{11}|^2$ and $T = |S_{21}|^2$, respectively. Then, reflection attenuation (SE_R) and absorption attenuation (SE_A) were obtained using $SE_R = -10\log(1-R)$ and $SE_A = -10\log\left(\frac{T}{1}-R\right)$. The total EMI SE ($SE_T$) was calculated by $SE_T = SE_R + SE_A$. A thermal imaging camera (E60, FLIR) was used to display and record the temperature of the sample. The solar simulator (CEL-HXF300) was used to simulate the energy produced by the Sun in reality.

■ ASSOCIATED CONTENT

Supporting Information

The Supporting Information is available free of charge at https://pubs.acs.org/doi/10.1021/acsami.1c07976.

> Tyndall effect; FTIR spectra; SEM images of Mx textiles and SiO_2/PDMS coating; EDS of PDA-grafted textile; water contact angles of Mx@SPF and Mx@F textiles; comparison between the theoretical SE_T value and experimental results; electrical conductivity of Mx textiles; absorption spectra; the mass change of water for Mx@SPF textiles with reservoir under 1 sun; and comparison of EMI SE of various EMI shielding textiles (PDF)
>
> The water repellency of the SPF surface of the superhydrophobic textile (Movie S1) (MP4)
>
> M5@SPF textile has superhydrophobic properties while maintaining good air permeability (Movies S2 and S3) (MP4) (MP4)
>
> Self-cleaning performance of the surface of M5@F and M5@SPF textiles (Movie S4) (MP4)
>
> The mass change of water over time for the M3@SPF textile with reservoir (Movie S5) (MP5)

■ AUTHOR INFORMATION

Corresponding Author

Xianhu Liu − *College of Materials Science and Engineering, National Engineering Research Center for Advanced Polymer Processing Technology, Henan Province Industrial Technology Research Institute of Resources and Materials, Key Laboratory of Advanced Material Processing & Mold (Ministry of Education), Zhengzhou University, Zhengzhou 450002, China*; orcid.org/0000-0002-4975-3586; Email: xianhu.liu@zzu.edu.cn

Authors

En Li − *College of Materials Science and Engineering, National Engineering Research Center for Advanced Polymer Processing Technology, Henan Province Industrial Technology Research Institute of Resources and Materials, Key Laboratory of Advanced Material Processing & Mold (Ministry of Education), Zhengzhou University, Zhengzhou 450002, China*

Yamin Pan − *College of Materials Science and Engineering, National Engineering Research Center for Advanced Polymer Processing Technology, Henan Province Industrial Technology Research Institute of Resources and Materials, Key Laboratory of Advanced Material Processing & Mold (Ministry of Education), Zhengzhou University, Zhengzhou 450002, China*

Chunfeng Wang − *Beijing Institute of Nanoenergy and Nanosystems, Chinese Academy of Sciences, National Center for Nanoscience and Technology (NCNST), Beijing 100083, China*

Chuntai Liu − *College of Materials Science and Engineering, National Engineering Research Center for Advanced Polymer Processing Technology, Henan Province Industrial Technology Research Institute of Resources and Materials, Key Laboratory of Advanced Material Processing & Mold (Ministry of Education), Zhengzhou University, Zhengzhou 450002, China*; orcid.org/0000-0001-9751-6270

Changyu Shen − *College of Materials Science and Engineering, National Engineering Research Center for Advanced Polymer Processing Technology, Henan Province Industrial Technology Research Institute of Resources and Materials, Key Laboratory of Advanced Material Processing & Mold (Ministry of Education), Zhengzhou University, Zhengzhou 450002, China*

Caofeng Pan − *Beijing Institute of Nanoenergy and Nanosystems, Chinese Academy of Sciences, National Center for Nanoscience and Technology (NCNST), Beijing 100083, China*; orcid.org/0000-0001-6327-9692

Complete contact information is available at: https://pubs.acs.org/10.1021/acsami.1c07976

Author Contributions

§E.L. and Y.P. contributed equally to this study.

Notes

The authors declare no competing financial interest.

■ ACKNOWLEDGMENTS

The authors thank the National Natural Science Foundation of China (51803190), Provincial and Ministerial Co-construction of Collaborative Innovation Center Foundation for Resource Materials (zycl202004), and National Key R&D Program of China (2019YFA0706802) for financial support.

■ REFERENCES

(1) Ghosh, S.; Nitin, B.; Remanan, S.; Bhattacharjee, Y.; Ghorai, A.; Dey, T.; Das, T. K.; Das, N. C. A Multifunctional Smart Textile Derived from Merino Wool/Nylon Polymer Nanocomposites as Next Generation Microwave Absorber and Soft Touch Sensor. *ACS Appl. Mater. Interfaces* **2020**, *12*, 17988−18001.

(2) Lan, C.; Guo, M.; Li, C.; Qiu, Y.; Ma, Y.; Sun, J. Axial Alignment of Carbon Nanotubes on Fibers To Enable Highly Conductive Fabrics for Electromagnetic Interference Shielding. *ACS Appl. Mater. Interfaces* **2020**, *12*, 7477−7485.

(3) Weng, G.; Li, J.; Alhabeb, M.; Karpovich, C.; Wang, H.; Lipton, J.; Maleski, K.; Kong, J.; Shaulsky, E.; Elimelech, M.; Gogotsi, Y.; Taylor, A. D. Layer-by-Layer Assembly of Cross-Functional Semi-transparent MXene-Carbon Nanotubes Composite Films for Next-Generation Electromagnetic Interference Shielding. *Adv. Funct. Mater.* **2018**, *28*, No. 1803360.

(4) Lyu, L.; Liu, J.; Liu, H.; Liu, C.; Lu, Y.; Sun, K.; Fan, R.; Wang, N.; Lu, N.; Guo, Z.; Wujcik, E. K. An Overview of Electrically Conductive Polymer Nanocomposites toward Electromagnetic Interference Shielding. *Eng. Sci.* **2018**, *2*, 26−42.

(5) Jia, Y.; Sun, R.; Pan, Y.; Wang, X.; Zhai, Z.; Min, Z.; Zheng, G.; Liu, C.; Shen, C.; Liu, X. Flexible and Thin Multifunctional Waterborne Polyurethane/Ag Film for High-efficiency Electromagnetic Interference Shielding, Electro-thermal and Strain Sensing Performances. *Composites, Part B* **2021**, *210*, No. 108668.

(6) Weng, W.; Chen, P.; He, S.; Sun, X.; Peng, H. Smart Electronic Textiles. *Angew. Chem., Int. Ed.* **2016**, *55*, 6140−6169.

(7) Heo, J. S.; Eom, J.; Kim, Y. H.; Park, S. K. Recent Progress of Textile-Based Wearable Electronics: A Comprehensive Review of Materials, Devices, and Applications. *Small* **2018**, *14*, No. 1703034.

(8) Wang, Q.; Zhang, H.; Liu, J.; Zhao, S.; Xie, X.; Liu, L.; Yang, R.; Koratkar, N.; Yu, Z. Multifunctional and Water-Resistant MXene-Decorated Polyester Textiles with Outstanding Electromagnetic Interference Shielding and Joule Heating Performances. *Adv. Funct. Mater.* **2019**, *29*, No. 1806819.

(9) Lee, J.; Liu, Y.; Liu, Y.; Park, S.-J.; Park, M.; Kim, H. Y. Ultrahigh Electromagnetic Interference Shielding Performance of Lightweight, Flexible, and Highly Conductive Copper-clad Carbon Fiber Non-woven Fabrics. *J. Mater. Chem. C* **2017**, *5*, 7853−7861.

(10) Jia, L.; Ding, K.; Ma, R.; Wang, H.; Sun, W.; Yan, D.; Li, B.; Li, Z. Highly Conductive and Machine-Washable Textiles for Efficient Electromagnetic Interference Shielding. *Adv. Mater. Technol.* **2019**, *4*, No. 1800503.

(11) Zhang, Q.; Liang, Q.; Zhang, Z.; Kang, Z.; Liao, Q.; Ding, Y.; Ma, M.; Gao, F.; Zhao, X.; Zhang, Y. Electromagnetic Shielding Hybrid Nanogenerator for Health Monitoring and Protection. *Adv. Funct. Mater.* **2018**, *28*, No. 1703801.

(12) Yang, Z.; Pang, Y.; Han, X.; Yang, Y.; Ling, J.; Jian, M.; Zhang, Y.; Yang, Y.; Ren, T. Graphene Textile Strain Sensor with Negative Resistance Variation for Human Motion Detection. *ACS Nano* **2018**, *12*, 9134−9141.

(13) Yang, T.; Xie, D.; Li, Z.; Zhu, H. Recent Advances in Wearable Tactile Sensors: Materials, Sensing Mechanisms, and Device Performance. *Mater. Sci. Eng., R* **2017**, *115*, 1−37.

(14) Cui, Y.; Gong, H.; Wang, Y.; Li, D.; Bai, H. A Thermally Insulating Textile Inspired by Polar Bear Hair. *Adv. Mater.* **2018**, *30*, No. 1706807.

(15) Liu, Q.; Huang, J.; Zhang, J.; Hong, Y.; Wan, Y.; Wang, Q.; Gong, M.; Wu, Z.; Guo, C. F. Thermal, Waterproof, Breathable, and Antibacterial Cloth with a Nanoporous Structure. *ACS Appl. Mater. Interfaces* **2018**, *10*, 2026−2032.

(16) Guo, J.; Qu, Z.; Wang, X. A Reverse Thermal Cloak Design Method Based on Inverse Problem Theory. *ES Energy Environ.* **2020**, *7*, 71−83.

(17) Hu, L.; Pasta, M.; La Mantia, F.; Cui, L.; Jeong, S.; Deshazer, H. D.; Choi, J. W.; Han, S. M.; Cui, Y. Stretchable, Porous, and Conductive Energy Textiles. *Nano Lett.* **2010**, *10*, 708−714.

(18) Zhou, Z.; Panatdasirisuk, W.; Mathis, T. S.; Anasori, B.; Lu, C.; Zhang, X.; Liao, Z.; Gogotsi, Y.; Yang, S. Layer-by-layer Assembly of MXene and Carbon Nanotubes on Electrospun Polymer Films for Flexible Energy Storage. *Nanoscale* **2018**, *10*, 6005−6013.

(19) Jin, H.; Matsuhisa, N.; Lee, S.; Abbas, M.; Yokota, T.; Someya, T. Enhancing the Performance of Stretchable Conductors for E-Textiles by Controlled Ink Permeation. *Adv. Mater.* **2017**, *29*, No. 1605848.

(20) Zhang, L.; Fairbanks, M.; Andrew, T. L. Rugged Textile Electrodes for Wearable Devices Obtained by Vapor Coating Off-the-Shelf, Plain-Woven Fabrics. *Adv. Funct. Mater.* **2017**, *27*, No. 1700415.

(21) Yang, Y.; Huang, Q.; Niu, L.; Wang, D.; Yan, C.; She, Y.; Zheng, Z. Waterproof, Ultrahigh Areal-Capacitance, Wearable Supercapacitor Fabrics. *Adv. Mater.* **2017**, *29*, No. 1606679.

(22) Lu, W.; Yu, P.; Jian, M.; Wang, H.; Wang, H.; Liang, X.; Zhang, Y. Molybdenum Disulfide Nanosheets Aligned Vertically on Carbonized Silk Fabric as Smart Textile for Wearable Pressure-Sensing and Energy Devices. *ACS Appl. Mater. Interfaces* **2020**, *12*, 11825−11832.

(23) Tsai, P. Performance of Masks and Discussion of the Inactivation of SARS-CoV-2. *Eng. Sci.* **2020**, *10*, 1−7.

(24) Jiang, Q.; Lu, L. COVID-19: From Crude Oil to Medical Mask. *ES Mater. Manuf.* **2020**, *7*, 1−3.

(25) Zhao, H.; Hou, L.; Lu, Y. Electromagnetic Interference Shielding of Layered Linen Fabric/polypyrrole/nickel (LF/PPy/Ni) Composites. *Mater. Des.* **2016**, *95*, 97−106.

(26) Luo, J.; Wang, L.; Huang, X.; Li, B.; Guo, Z.; Song, X.; Lin, L.; Tang, L.; Xue, H.; Gao, J. Mechanically Durable, Highly Conductive, and Anticorrosive Composite Fabrics with Excellent Self-Cleaning Performance for High-Efficiency Electromagnetic Interference Shielding. *ACS Appl. Mater. Interfaces* **2019**, *11*, 10883−10894.

(27) Zhang, Q.; Xiao, X.; Wang, G.; Ming, X.; Liu, X.; Wang, H.; Yang, H.; Xu, W.; Wang, X. Silk-based Systems for Highly Efficient Photothermal Conversion under One Sun: Portability, Flexibility, and Durability. *J. Mater. Chem. A* **2018**, *6*, 17212−17219.

(28) Huang, X.; Li, B.; Wang, L.; Lai, X.; Xue, H.; Gao, J. Superhydrophilic, Underwater Superoleophobic, and Highly Stretchable Humidity and Chemical Vapor Sensors for Human Breath Detection. *ACS Appl. Mater. Interfaces* **2019**, *11*, 24533−24543.

(29) Xie, P.; Liu, Y.; Feng, M.; Niu, M.; Liu, C.; Wu, N.; Sui, K.; Patil, R. R.; Pan, D.; Guo, Z.; Fan, R. Hierarchically Porous Co/C Nanocomposites for Ultralight High-performance Microwave Absorption. *Adv. Compos. Hybrid Mater.* **2021**, *4*, 173−185.

(30) Wu, N.; Du, W.; Hu, Q.; Jiang, Q.; Vupputuri, S. Recent Development in Fabrication of Co Nanostructures and Their Carbon Nanocomposites for Electromagnetic Wave Absorption. *Eng. Sci.* **2020**, *13*, 11−23.

(31) Wang, X.; Liu, X.; Schubert, D. W. Highly Sensitive Ultrathin Flexible Thermoplastic Polyurethane/Carbon Black Fibrous Film Strain Sensor with Adjustable Scaffold Networks. *Nano-Micro Lett.* **2021**, *13*, No. 64.

(32) Feng, M.; Pan, Y.; Zhang, M.; Gao, Q.; Liu, C.; Shen, C.; Liu, X. Largely Improved Thermal Conductivity of HDPE Composites by Building a 3D Hybrid Fillers Network. *Compos. Sci. Technol.* **2021**, *206*, No. 108666.

(33) Liu, L.; Chen, W.; Zhang, H.; Wang, Q.; Guan, F.; Yu, Z. Flexible and Multifunctional Silk Textiles with Biomimetic Leaf-Like MXene/Silver Nanowire Nanostructures for Electromagnetic Interference Shielding, Humidity Monitoring, and Self-Derived Hydrophobicity. *Adv. Funct. Mater.* **2019**, *29*, No. 1905197.

(34) Liu, L. X.; Chen, W.; Zhang, H. B.; Wang, Q. W.; Guan, F.; Yu, Z. Z. Flexible and Multifunctional Silk Textiles with Biomimetic Leaf-Like MXene/Silver Nanowire Nanostructures for Electromagnetic Interference Shielding, Humidity Monitoring, and Self-Derived Hydrophobicity. *Adv. Funct. Mater.* **2019**, *29*, No. 1905197.

(35) Gogotsi, Y.; Anasori, B. The Rise of MXenes. *ACS Nano* **2019**, *13*, 8491−8494.

(36) Du, C.; Sun, X.; Yu, H.; Fang, W.; Jing, Y.; Wang, Y.; Li, S.; Liu, X.; Yan, Q. V4C3Tx MXene: A Promising Active Substrate for Reactive Surface Modification and The Enhanced Electrocatalytic Oxygen Evolution Activity. *InfoMat* **2020**, *2*, 950−959.

(37) Cheng, H.; Pan, Y.; Chen, Q.; Che, R.; Zheng, G.; Liu, C.; Shen, C.; Liu, X. Ultrathin Flexible Poly(vinylidene fluoride)/MXene/silver Nanowire Film with Outstanding Specific EMI Shielding and High Heat Dissipation. *Adv. Compos. Hybrid Mater.* **2021**, 1−9.

(38) Gao, Q.; Pan, Y.; Zheng, G.; Liu, C.; Shen, C.; Liu, X. Flexible Multilayered MXene/thermoplastic Polyurethane Films with Excellent Electromagnetic Interference Shielding, Thermal Conductivity, and Management Performances. *Adv. Compos. Hybrid Mater.* **2021**, *4*, 274−285.

(39) Wang, Y.; Liu, Y.; Wang, C.; Liu, H.; Zhang, J.; Lin, J.; Fan, J.; Ding, T.; Ryu, J. E.; Guo, Z. Significantly Enhanced Ultrathin NiCo-based MOF Nanosheet Electrodes Hybrided with Ti3C2Tx MXene for High Performance Asymmetric Supercapacitor. *Eng. Sci.* **2020**, *9*, 50−59.

(40) Akuzum, B.; Maleski, K.; Anasori, B.; Lelyukh, P.; Alvarez, N. J.; Kumbur, E. C.; Gogotsi, Y. Rheological Characteristics of 2D Titanium Carbide (MXene) Dispersions: A Guide for Processing MXenes. *ACS Nano* **2018**, *12*, 2685−2694.

(41) Luo, J.; Gao, S.; Luo, H.; Wang, L.; Huang, X.; Guo, Z.; Lai, X.; Lin, L.; Li, R. K. Y.; Gao, J. Superhydrophobic and Breathable Smart MXene-based Textile for Multifunctional Wearable Sensing Electronics. *Chem. Eng. J.* **2021**, *406*, No. 126898.

(42) Huang, X.; Zhang, S.; Xiao, W.; Luo, J.; Li, B.; Wang, L.; Xue, H.; Gao, J. Flexible PDA@ACNTs Decorated Polymer Nanofiber Composite with Superhydrophilicity and Underwater Superoleophobicity for Efficient Separation of Oil-in-water Emulsion. *J. Membr. Sci.* **2020**, *614*, No. 118500.

(43) Cassie, A. B. D.; Baxter, S. Wettability of Porous Surfaces. *Trans. Faraday Soc.* **1944**, *40*, 546−551.

(44) Su, M.; Pan, Y.; Zheng, G.; Liu, C.; Shen, C.; Liu, X. An Ultralight, Superhydrophobic and Thermal Insulation Ultra-high Molecular Weight Polyethylene Foam. *Polymer* **2021**, *218*, No. 123528.

(45) Chen, J.; Yuan, L.; Shi, C.; Wu, C.; Long, Z.; Qiao, H.; Wang, K.; Fan, Q. H. Nature-Inspired Hierarchical Protrusion Structure Construction for Washable and Wear-Resistant Superhydrophobic Textiles with Self-Cleaning Ability. *ACS Appl. Mater. Interfaces* **2021**, *13*, 18142−18151.

(46) Zhang, X.; Liu, Z.; Li, Y.; Cui, Y.; Wang, H.; Wang, J. Durable Superhydrophobic Surface Prepared by Designing “Micro-eggshell” and “Web-like” Structures. *Chem. Eng. J.* **2020**, *392*, No. 123741.

(47) Wang, H.; Zhang, Z.; Zheng, J.; Zhao, J.; Liang, Y.; Li, X.; Ren, L. Multifunctional Superhydrophobic Surface with Dynamically Controllable Micro/nanostructures for Droplet Manipulation and Friction Control. *Chem. Eng. J.* **2020**, *417*, No. 127944.

(48) Zhang, X.; Liu, Z.; Li, Y.; Wang, C.; Zhu, Y.; Wang, H.; Wang, J. Robust Superhydrophobic Epoxy Composite Coating Prepared by Dual Interfacial Enhancement. *Chem. Eng. J.* **2019**, *371*, 276−285.

(49) Iqbal, A.; Sambyal, P.; Koo, C. M. 2D MXenes for Electromagnetic Shielding: A Review. *Adv. Funct. Mater.* **2020**, *30*, No. 2000883.

(50) Ma, Z.; Kang, S.; Ma, J.; Shao, L.; Wei, A.; Liang, C.; Gu, J.; Yang, B.; Dong, D.; Wei, L.; Ji, Z. High-Performance and Rapid-Response Electrical Heaters Based on Ultraflexible, Heat-Resistant, and Mechanically Strong Aramid Nanofiber/Ag Nanowire Nanocomposite Papers. *ACS Nano* **2019**, *13*, 7578−7590.

(51) Iqbal, A.; Shahzad, F.; Hantanasirisakul, K.; Kim, M.-K.; Kwon, J.; Hong, J.; Kim, H.; Kim, D.; Gogotsi, Y.; Koo, C. M. Anomalous Absorption of Electromagnetic Waves by 2D Transition Metal Carbonitride Ti3CNT x (MXene). *Science* **2020**, *369*, 446−450.

(52) Shahzad, F.; Alhabeb, M.; Hatter, C. B.; Anasori, B.; Man Hong, S.; Koo, C. M.; Gogotsi, Y. Electromagnetic Interference Shielding with 2D Transition Metal Carbides (MXenes). *Science* **2016**, *353*, 1137−1140.

(53) Chen, H.; Wen, Y.; Qi, Y.; Zhao, Q.; Qu, L.; Li, C. Pristine Titanium Carbide MXene Films with Environmentally Stable Conductivity and Superior Mechanical Strength. *Adv. Funct. Mater.* **2020**, *30*, No. 1906996.

(54) Ma, Z.; Kang, S.; Ma, J.; Shao, L.; Zhang, Y.; Liu, C.; Wei, A.; Xiang, X.; Wei, L.; Gu, J. Ultraflexible and Mechanically Strong Double-Layered Aramid Nanofiber−Ti3C2Tx MXene/Silver Nanowire Nanocomposite Papers for High-Performance Electromagnetic Interference Shielding. *ACS Nano* **2020**, *14*, 8368−8382.

(55) Zhao, X.; Wang, L.; Tang, C.; Zha, X.; Liu, Y.; Su, B.; Ke, K.; Bao, R.; Yang, M.; Yang, W. Smart Ti3C2Tx MXene Fabric with Fast Humidity Response and Joule Heating for Healthcare and Medical Therapy Applications. *ACS Nano* **2020**, *14*, 8793−8805.

(56) Wang, L.; Gong, Q.; Zhan, S.; Jiang, L.; Zheng, Y. Robust Anti-Icing Performance of a Flexible Superhydrophobic Surface. *Adv. Mater.* **2016**, *28*, 7729−7735.

(57) Li, Y.; Jin, X.; Zheng, Y.; Li, W.; Zheng, F.; Wang, W.; Lin, T.; Zhu, Z. Tunable Water Delivery in Carbon-Coated Fabrics for High-Efficiency Solar Vapor Generation. *ACS Appl. Mater. Interfaces* **2019**, *11*, 46938−46946.

(58) Li, H.; He, Y.; Hu, Y.; Wang, X. Commercially Available Activated Carbon Fiber Felt Enables Efficient Solar Steam Generation. *ACS Appl. Mater. Interfaces* **2018**, *10*, 9362−9368.

(59) Li, E.; Pan, Y.; Wang, C.; Liu, C.; Shen, C.; Pan, C.; Liu, X. Multifunctional and Superhydrophobic Cellulose Composite Paper for Electromagnetic Shielding, Hydraulic Triboelectric Nanogenerator and Joule Heating Applications. *Chem. Eng. J.* **2021**, *420*, No. 129864.